

# C-MambaPose: A Physics-Informed Complex Mamba Framework for Cross-Environment WiFi Human Pose Estimation

Phuc Nguyen H.

*Abstract*—Human pose estimation (HPE) utilizing wireless WiFi signals has emerged as a promising technology owing to its device-free nature, privacy preservation, and robustness against occlusion and poor lighting. However, existing methods often overlook the physical complex phase information of WiFi signals and fail to generalize across diverse environments due to severe domain shifts. In this paper, we present C-MambaPose, a physics-informed complex-valued Mamba-GraFormer hybrid framework for robust cross-environment WiFi-based 3D HPE. Our framework first sanitizes raw WiFi Channel State Information (CSI) phase errors and constructs a phase-preserving complex-valued representation. We then employ a Spatiotemporal Complex Mamba encoder with a dynamic selective receptive field to capture fine-grained phase dynamics. A cross-attention joint-query mapper maps the unstructured sequence tokens to human joints, which are decoded by a Graph Convolutional Network (GCN) to predict anatomically coherent 3D coordinates. Extensive evaluations on the MM-Fi dataset show that C-MambaPose achieves competitive or superior performance to state-of-the-art baselines across all settings, setting a new state-of-the-art specifically on the challenging cross-environment split, requiring only 3.78 M parameters—an 83.1% reduction compared to GraphPose-Fi [1] and an 85.7% reduction compared to MetaFi++ [2], while maintaining a comparable size to DT-Pose [3] (which is only 18% smaller) but achieving significantly superior performance without requiring any pretraining. Our code is publicly available at <https://github.com/phucngvinuni/cmambose.git>.

*Index Terms*—Human Pose Estimation, WiFi Sensing, Mamba, Graph Convolutional Networks

## I. INTRODUCTION

**3**D Human Pose Estimation (HPE) is a cornerstone technology in computer vision and ubiquitous computing, enabling diverse applications such as smart home automation, healthcare monitoring, and human-computer interaction. While traditional camera-based approaches achieve high accuracy, they face severe challenges in real-world deployment, including susceptibility to poor lighting conditions, physical occlusions, and significant privacy concerns. On the other hand, wearable sensor-based methods offer high privacy but are inherently intrusive, requiring subjects to constantly wear specialized devices.

To address these limitations, WiFi-based HPE utilizing Channel State Information (CSI) has emerged as a promising non-invasive and privacy-preserving alternative [4], with recent developments like WiFlow [5] investigating lightweight architectures with spatio-temporal decoupling for continuous pose tracking. CSI measurements capture the multipath reflections

of wireless signals off the human body, encoding fine-grained spatial and temporal dynamics. However, existing WiFi-based HPE methods still struggle with two key challenges:

First, most current architectures either discard the complex-valued nature of WiFi CSI signals by focusing solely on amplitude [2], or treat real and imaginary parts as independent real channels. Raw CSI phase is heavily corrupted by sampling frequency offset (SFO) and carrier frequency offset (CFO) errors. Simple phase removal or naive handling discards the pristine phase relationships (Doppler shifts) that are physically coupled with body motions. Preserving the physical complex-valued relationships is crucial for capturing minor displacements.

Second, existing models often suffer from high computational complexity and poor generalization under cross-environment settings. Due to the high sensitivity of WiFi propagation to room layout, furniture, and multipath scattering, models trained in one room experience severe domain shift when tested in another. Although domain adaptation frameworks like AdaWiFi [6] have been proposed for collaborative WiFi sensing, generalization remains challenging. Current state-of-the-art models like MetaFi++ [2] rely on large CNN/Transformer backbones (e.g., 26.52 M parameters), which easily overfit to background multipath noise. While newer architectures like DT-Pose [3] lower parameter size to 3.20 M, they still lack explicit physical skeleton regularization, leading to anatomically invalid pose predictions in unseen environments.

To overcome these limitations, we propose **C-MambaPose**, a physics-informed complex-valued Mamba-GraFormer hybrid framework designed specifically for cross-environment WiFi-based 3D HPE. Our framework introduces a complex-valued patchification pipeline that sanitizes raw CSI phase errors while keeping the complex signal intact. We apply a complex 2D convolution and a phase-preserving activation function (Complex-ModReLU) to map the signal into an intermediate feature space without losing phase coherence. To adaptively capture motions across different speeds, we introduce a Complex Dynamic Selective Kernel Convolution (Complex-DSKConv) which dynamically reweights branches with varying dilations.

For spatiotemporal sequence modeling, we employ a Spatiotemporal Complex Mamba encoder. State-space models (SSMs) have recently shown great promise as lightweight, linear-time sequence processors for wireless sensing, as demonstrated in SenseMamba [7] and TF-Mamba [8] for activity recognition, and MambaCSP [9] for channel prediction.

Building on these advantages and inspired by the complex-valued state update principles in Mamba-3 [10], we leverage selective complex-valued SSMS to capture long-range temporal phase and amplitude dynamics with linear complexity. To map these unstructured sequence tokens to the human skeleton, we define learnable joint-query embeddings updated via multi-head cross-attention. Finally, these features are decoded by a Graph Convolutional Network (GCN) decoder (GraFormer), which explicitly enforces physical bone length and skeletal topology constraints. This regularization prevents unnatural bone stretching and significantly reduces parameter count.

In summary, the key contributions of this work are:

- We propose a physics-informed complex-valued patchification pipeline utilizing Complex-ModReLU and Complex-DSKConv, which explicitly preserves WiFi phase dynamics and adaptively scales the receptive field.
- We introduce a hybrid Mamba-GraFormer architecture that combines the long-range sequential capacity of selective state-space models with the structural prior of GCNs, enabling high generalization with extreme parameter efficiency.
- C-MambaPose achieves competitive or superior results on the MM-Fi dataset. Notably, on the challenging cross-environment split (Setting 3), it reduces MPJPE to **298.5 mm** with an extremely lightweight parameter footprint (comparable to DT-Pose [3])-an **83.1%** reduction compared to GraphPose-Fi [1]. C-MambaPose achieves significantly superior performance without requiring any pretraining.

## II. METHODOLOGY

In this section, we present the proposed C-MambaPose architecture, a Mamba-GraFormer hybrid framework designed for robust WiFi-based 3D human pose estimation (HPE), as illustrated in Fig. 1. The overall architecture consists of three main stages: (1) CSI Phase Sanitization and Decoupled Formulation, (2) Spatiotemporal Complex Late-Fusion Mamba Encoder, and (3) Cross-Attention Joint-Query Mapping followed by the Regularized GraFormer Decoder.

### A. CSI Phase Sanitization and Decoupled Formulation

Unlike conventional architectures that either discard phase information or treat raw complex Channel State Information (CSI) variables naively, our framework explicitly leverages the physical coupling between phase variations and human body motion. The raw complex CSI matrix obtained from a WiFi packet is represented as  $\mathbf{H} \in \mathbb{C}^{A \times S \times T}$ , where  $A$  denotes the receiver antenna count,  $S$  the subcarrier count, and  $T$  the frame sequence length.

Due to sampling frequency offset (SFO) and carrier frequency offset (CFO) between the transmitter and receiver clocks, as well as phase-locked loop (PLL) phase noise, the raw phase measurements  $\Theta^{\text{raw}} \in \mathbb{R}^{A \times S \times T}$  are corrupted by severe linear errors. To extract the sanitized phase  $\Theta_{\text{clean}}$ , we first apply phase unwrapping along the subcarrier axis  $S$  to resolve  $2\pi$  phase ambiguities:

$$\theta_{i,s,t}^{\text{unwrapped}} = \text{unwrap}(\theta_{i,s,t}^{\text{raw}}), \quad (1)$$

where  $i \in \{1, \dots, A\}$  is the antenna index,  $s \in \{0, \dots, N-1\}$  is the subcarrier index with  $N = 114$  subcarriers, and  $t$  is the time step. The unwrapped phase is modeled as:

$$\theta_{i,s,t}^{\text{unwrapped}} = s \cdot m_{i,t} + c_{i,t} + \theta_{i,s,t}^{\text{clean}}, \quad (2)$$

where  $m_{i,t}$  is the phase slope induced by SFO and CFO, and  $c_{i,t}$  is the constant phase offset. We estimate these parameters via least-squares linear regression:

$$m_{i,t} = \frac{N \sum_{s=0}^{N-1} s \cdot \theta_{i,s,t}^{\text{unwrapped}} - \left( \sum_{s=0}^{N-1} s \right) \left( \sum_{s=0}^{N-1} \theta_{i,s,t}^{\text{unwrapped}} \right)}{N \sum_{s=0}^{N-1} s^2 - \left( \sum_{s=0}^{N-1} s \right)^2}, \quad (3)$$

$$c_{i,t} = \frac{\sum_{s=0}^{N-1} \theta_{i,s,t}^{\text{unwrapped}} - m_{i,t} \sum_{s=0}^{N-1} s}{N}. \quad (4)$$

The sanitized, clean phase  $\theta_{i,s,t}^{\text{clean}}$  is then obtained by subtracting the linear fit from the unwrapped phase:

$$\theta_{i,s,t}^{\text{clean}} = \theta_{i,s,t}^{\text{unwrapped}} - (s \cdot m_{i,t} + c_{i,t}), \quad (5)$$

which defines the clean phase tensor  $\Theta_{\text{clean}} \in \mathbb{R}^{A \times S \times T}$ .

Rather than early fusing the amplitude and phase into a single complex tensor, we formulate a decoupled representation to allow specialized feature extraction:

- 1) **Sanitized Unit-Circle Complex Phase:** To preserve phase coherence and raw angular relationships, the phase is mapped onto the unit circle in the complex domain:

$$\mathbf{P} = \cos(\Theta_{\text{clean}}) + j \sin(\Theta_{\text{clean}}) \in \mathbb{C}^{A \times S \times T}. \quad (6)$$

To accommodate standard deep learning architectures, we represent  $\mathbf{P}$  as a real-valued tensor  $\mathbf{X}_{\text{phase}} \in \mathbb{R}^{C_{\text{in}}^{\text{p}} \times S \times T}$  by concatenating the real and imaginary parts along the antenna channel dimension:

$$\mathbf{X}_{\text{phase}} = [\cos(\Theta_{\text{clean}}); \sin(\Theta_{\text{clean}})]. \quad (7)$$

For a system with  $A = 3$  receiver antennas, this yields  $C_{\text{in}}^{\text{p}} = 6$  input channels in the real domain (representing the real and imaginary components for all receiver antennas).

- 2) **Normalized CSI Amplitude:** The raw CSI amplitude  $\mathbf{A} = |\mathbf{H}| \in \mathbb{R}^{A \times S \times T}$  is standardized sample-wise to eliminate static environmental domain mismatches:

$$\mathbf{X}_{\text{amp}} = \frac{\mathbf{A} - \mu_{\mathbf{A}}}{\sigma_{\mathbf{A}} + \eta} \in \mathbb{R}^{C_{\text{in}}^{\text{a}} \times S \times T}, \quad (8)$$

where  $\mu_{\mathbf{A}}$  and  $\sigma_{\mathbf{A}}$  are the mean and standard deviation of the amplitude over all subcarriers and time steps,  $C_{\text{in}}^{\text{a}}$  is the amplitude input channel dimension (which is equal to the receiver antenna count  $A = 3$ ), and  $\eta$  is a small stabilizing constant.

### B. Spatiotemporal Complex Late-Fusion Mamba Encoder

We propose a decoupled spatiotemporal encoder that extracts features from the phase and amplitude inputs using parallel branches, performs late fusion in the complex domain, and models long-range dynamics using a regularized Complex Mamba sequence processor.

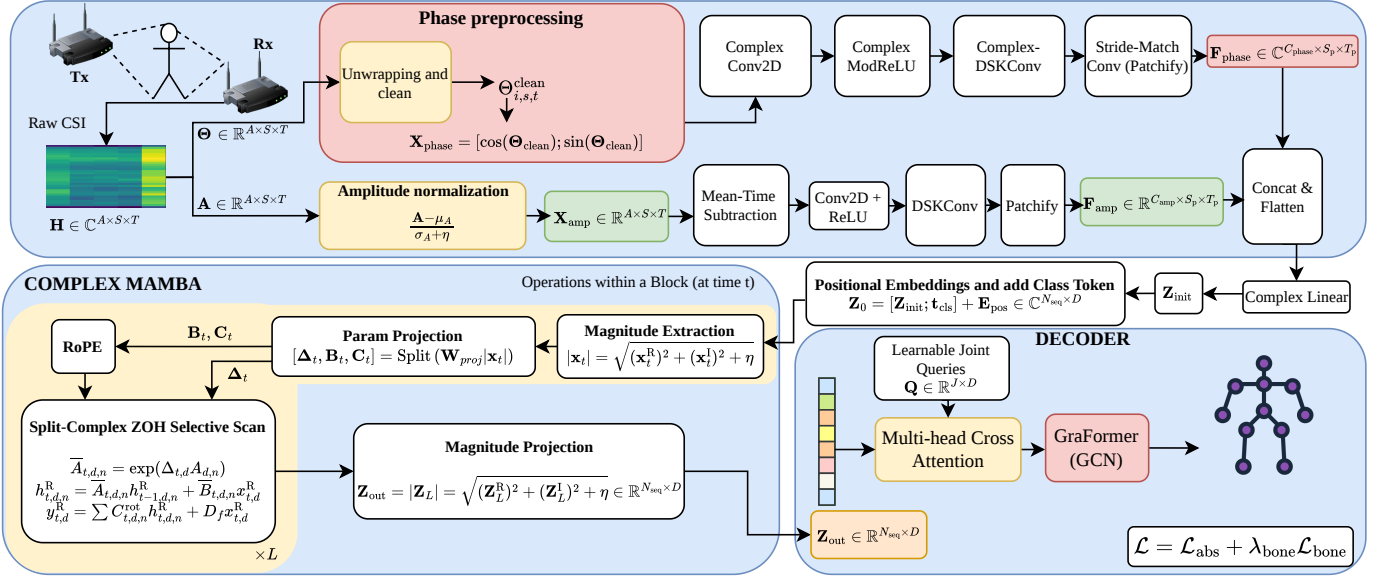


Fig. 1: Overview of C-MambaPose framework. Raw WiFi CSI signals are decoupled into phase and amplitude. The parallel complex phase branch uses Complex-ModReLU and Complex-DSKConv for phase-coherent feature learning, while the amplitude branch standardizes signals. Both branches are fused in complex space to form a spatiotemporal representation processed by Complex Mamba sequence blocks. A cross-attention joint-query mapper routes sequence tokens to joint queries, which are decoded by a GCN GraFormer regularized by kinematic bone length constraints.

1) *Parallel Feature Extraction*: The sanitized phase input  $\mathbf{X}_{\text{phase}}$  and normalized amplitude input  $\mathbf{X}_{\text{amp}}$  are processed by parallel feature extraction branches:

- **Phase Encoder Branch**: A complex-valued two-dimensional (2D) convolution projects  $\mathbf{X}_{\text{phase}}$  into a complex hidden space:

$$\mathbf{Z}_{\text{phase}} = \mathbf{W}_{\text{conv}}^{\text{p}} \otimes \mathbf{X}_{\text{phase}} + \mathbf{b}_{\text{conv}}^{\text{p}} \in \mathbb{C}^{C_{\text{phase}} \times S \times T}, \quad (9)$$

where  $\otimes$  denotes the complex convolution operator, and  $C_{\text{phase}}$  represents the complex channel dimension of the phase branch. Non-linearity is introduced using the magnitude-dependent Complex-ModReLU activation [11]:

$$\mathbf{U}_{\text{phase}} = \max(0, |\mathbf{Z}_{\text{phase}}| + \mathbf{b}_{\text{act}}^{\text{p}}) \odot \frac{\mathbf{Z}_{\text{phase}}}{|\mathbf{Z}_{\text{phase}}| + \eta}, \quad (10)$$

where  $|\cdot|$  is the element-wise magnitude. We then apply a Complex Dynamic Selective Kernel Convolution (Complex-DSKConv, which adapts Selective Kernel Networks [12] to the complex domain) to adaptively adjust the receptive field under different motion speeds. Specifically, for a set of  $B$  parallel branches with different kernel dilations, let  $\mathbf{U}_b = \mathbf{U}_b^{\text{r}} + j\mathbf{U}_b^{\text{i}} \in \mathbb{C}^{C_{\text{phase}} \times S \times T}$  denote the complex activation output of the  $b$ -th branch ( $b \in \{1, \dots, B\}$ ). The sum of all branch activations is computed as:

$$\mathbf{U}_{\text{sum}} = \sum_{b=1}^B \mathbf{U}_b \in \mathbb{C}^{C_{\text{phase}} \times S \times T}. \quad (11)$$

We compute the magnitude of this sum to extract a joint phase-amplitude envelope:

$$|\mathbf{U}_{\text{sum}}| = \sqrt{(\mathbf{U}_{\text{sum}}^{\text{r}})^2 + (\mathbf{U}_{\text{sum}}^{\text{i}})^2 + \eta} \in \mathbb{R}^{C_{\text{phase}} \times S \times T}. \quad (12)$$

A global spatial channel-wise descriptor  $\mathbf{s} \in \mathbb{R}^{C_{\text{phase}}}$  is computed via Global Average Pooling (GAP) of  $|\mathbf{U}_{\text{sum}}|$ :

$$s_c = \frac{1}{S \times T} \sum_{i=1}^S \sum_{t=1}^T |\mathbf{U}_{\text{sum}}|_{c,i,t}. \quad (13)$$

A bottleneck projection is applied to generate a compact feature vector  $\mathbf{z} = \text{ReLU}(\text{BN}(\mathbf{W}_{1s})) \in \mathbb{R}^d$ , where  $d = C_{\text{phase}}/r$  with reduction ratio  $r$ , and BN represents Batch Normalization. For each branch  $b$ , a soft attention weight vector  $\alpha_b \in \mathbb{R}^{C_{\text{phase}}}$  is computed using a softmax activation across all branches:

$$\alpha_{b,c} = \frac{\exp(\mathbf{W}_{2,b,c}\mathbf{z})}{\sum_{k=1}^B \exp(\mathbf{W}_{2,k,c}\mathbf{z})}, \quad (14)$$

where  $\mathbf{W}_{2,b}$  is the projection matrix for branch  $b$ . The final selected complex representation is computed as a weighted sum of the branch outputs:

$$\mathbf{U}_{\text{select}} = \sum_{b=1}^B \alpha_b \odot \mathbf{U}_b \in \mathbb{C}^{C_{\text{phase}} \times S \times T}, \quad (15)$$

where  $\odot$  denotes channel-wise multiplication. This is followed by a stride-matching complex convolution to generate complex-valued phase patch tokens  $\mathbf{F}_{\text{phase}} \in \mathbb{C}^{C_{\text{phase}} \times S_p \times T_p}$ .

- **Amplitude Encoder Branch**: In parallel,  $\mathbf{X}_{\text{amp}}$  is dynamically normalized to eliminate temporal environmental shifts:

$$\mathbf{X}_{\text{amp}}' = \mathbf{X}_{\text{amp}} - \text{mean}_t(\mathbf{X}_{\text{amp}}). \quad (16)$$

This is passed through a real-valued 2D convolution, a standard ReLU activation, a real-valued DSKConv, and

a patchifying convolution to yield real-valued amplitude patch tokens  $\mathbf{F}_{\text{amp}} \in \mathbb{R}^{C_{\text{amp}} \times S_p \times T_p}$ , where  $C_{\text{amp}}$  represents the channel dimension of the amplitude branch.

2) *Late Fusion in Complex Space*: To merge the decoupled streams while preserving phase-amplitude relations, we project the real amplitude tokens  $\mathbf{F}_{\text{amp}}$  to the complex domain by setting their imaginary part to zero:

$$\mathbf{F}'_{\text{amp}} = \mathbf{F}_{\text{amp}} + j\mathbf{0} \in \mathbb{C}^{C_{\text{amp}} \times S_p \times T_p}. \quad (17)$$

We split the real and imaginary parts of the phase stream:

$$\mathbf{F}_{\text{phase}} = \mathbf{F}_{\text{phase}}^{\text{R}} + j\mathbf{F}_{\text{phase}}^{\text{I}}, \quad (18)$$

where  $\mathbf{F}_{\text{phase}}^{\text{R}}, \mathbf{F}_{\text{phase}}^{\text{I}} \in \mathbb{R}^{C_{\text{phase}} \times S_p \times T_p}$ . The fused complex representation  $\mathbf{F}_{\text{fused}} = \mathbf{F}_{\text{fused}}^{\text{R}} + j\mathbf{F}_{\text{fused}}^{\text{I}} \in \mathbb{C}^{C_{\text{fused}} \times S_p \times T_p}$  (where  $C_{\text{fused}} = C_{\text{phase}} + C_{\text{amp}}$ ) is constructed by concatenating the components along the channel dimension:

$$\mathbf{F}_{\text{fused}}^{\text{R}} = [\mathbf{F}_{\text{phase}}^{\text{R}}; \mathbf{F}_{\text{amp}}], \quad \mathbf{F}_{\text{fused}}^{\text{I}} = [\mathbf{F}_{\text{phase}}^{\text{I}}; \mathbf{0}]. \quad (19)$$

The fused representation contains  $C_{\text{fused}}$  complex channels. The tokens are flattened spatiotemporally into a sequence of length  $N_p = S_p \times T_p$  and projected to the encoder embedding dimension  $D$  via a complex-valued linear layer:

$$\mathbf{Z}_{\text{init}} = \text{ComplexLinear}(\mathbf{F}_{\text{fused}}) \in \mathbb{C}^{N_p \times D}. \quad (20)$$

A Complex Layer Normalization is applied, and 1D complex positional embeddings  $\mathbf{E}_{\text{pos}}$  along with a class token  $\mathbf{t}_{\text{cls}}$  are added:

$$\mathbf{Z}_0 = [\mathbf{Z}_{\text{init}}; \mathbf{t}_{\text{cls}}] + \mathbf{E}_{\text{pos}} \in \mathbb{C}^{N_{\text{seq}} \times D}, \quad (21)$$

where  $N_{\text{seq}} = N_p + 1$  is the total sequence length. The class token  $\mathbf{t}_{\text{cls}}$  aggregates global sequence context during Complex Mamba state transitions and is excluded from the GCN joint-query mapping in the decoder stage to focus on local joint-specific spatiotemporal features.

3) *Sequence Processing with Regularized Complex Mamba*: The fused sequence  $\mathbf{Z}_0 \in \mathbb{C}^{N_{\text{seq}} \times D}$  represents a complex-valued state representation containing both sanitized phase dynamics and amplitude envelopes. To model the spatiotemporal motion sequences under linear computational complexity, we process  $\mathbf{Z}_0$  through  $L$  layers of spatiotemporal Complex Mamba blocks.

Each Complex Mamba layer is designed to operate on complex-valued sequences. Let  $\mathbf{x}_t = \mathbf{x}_t^{\text{R}} + j\mathbf{x}_t^{\text{I}} \in \mathbb{C}^{D_{\text{inner}}}$  be the complex input to the Selective State Space Model (SSM) at time step  $t$ , where  $D_{\text{inner}}$  represents the expanded inner dimension of the SSM block (e.g.,  $D_{\text{inner}} = E \cdot D$  with expansion factor  $E$ ). The core mathematical operations are detailed below:

a) *SSM Parameter Projection via Signal Magnitude*: To dynamically adjust the sequence receptive field based on the input signal, the selective parameters—including the step size  $\Delta_t \in \mathbb{R}^{D_{\text{inner}}}$  and the state projection vectors  $\mathbf{B}_t, \mathbf{C}_t \in \mathbb{R}^{D_{\text{state}}}$ —are projected from the physical signal envelope (magnitude) of the complex input. This design ensures that the discretization and state updates are physically driven by the strength of the body motion reflections:

$$|\mathbf{x}_t| = \sqrt{(\mathbf{x}_t^{\text{R}})^2 + (\mathbf{x}_t^{\text{I}})^2 + \eta} \in \mathbb{R}^{D_{\text{inner}}}, \quad (22)$$

$$[\Delta_t, \mathbf{B}_t, \mathbf{C}_t] = \text{Split}(\mathbf{W}_{\text{proj}}|\mathbf{x}_t|), \quad (23)$$

where  $\mathbf{W}_{\text{proj}}$  is a real-valued projection matrix. The step size  $\Delta_t$  is discretized using a Softplus activation:  $\Delta_t = \text{softplus}(\mathbf{W}_{\Delta}\Delta_t + \mathbf{b}_{\Delta})$ .

b) *State Parameter Rotary Position Embeddings (RoPE)*: To explicitly inject relative spatiotemporal distance priors into the sequence model, we apply Rotary Position Embeddings (RoPE) directly to the time-varying state parameters  $\mathbf{B}_t$  and  $\mathbf{C}_t$  before state execution. This allows the state transitions to be position-aware. For a  $D_{\text{state}}$ -dimensional real vector  $\mathbf{v}_t$  (representing  $\mathbf{B}_t$  or  $\mathbf{C}_t$ ), we group adjacent elements into real-imaginary pairs and rotate them at position  $t$ :

$$\mathbf{v}_{t,2k}^{\text{rot}} = \mathbf{v}_{t,2k} \cos(t\theta_k) - \mathbf{v}_{t,2k+1} \sin(t\theta_k), \quad (24)$$

$$\mathbf{v}_{t,2k+1}^{\text{rot}} = \mathbf{v}_{t,2k} \sin(t\theta_k) + \mathbf{v}_{t,2k+1} \cos(t\theta_k), \quad (25)$$

where the frequency base is  $\theta_k = \theta_{\text{base}}^{-2k/D_{\text{state}}}$  for  $k \in \{0, \dots, D_{\text{state}}/2 - 1\}$ , with  $\theta_{\text{base}}$  being a constant frequency base. This produces position-encoded matrices  $\mathbf{B}_t^{\text{rot}}$  and  $\mathbf{C}_t^{\text{rot}}$ .

c) *Split-Complex Selective Scan Discretization*: The selective state matrix  $\mathbf{A} \in \mathbb{R}^{D_{\text{inner}} \times D_{\text{state}}}$  and the position-encoded input matrix  $\mathbf{B}_t^{\text{rot}}$  are discretized using the Zero-Order Hold (ZOH) assumption: Since the state matrix  $\mathbf{A}$  in selective state-space models is diagonal (or independent per channel), the matrix exponentiation and inverse operations are performed element-wise. For each channel index  $d \in \{1, \dots, D_{\text{inner}}\}$  and state parameter index  $n \in \{1, \dots, D_{\text{state}}\}$ , the ZOH discretization is defined as:

$$\bar{A}_{t,d,n} = \exp(\Delta_{t,d}A_{d,n}), \quad (26)$$

$$\bar{B}_{t,d,n} = (\Delta_{t,d}A_{d,n})^{-1}(\exp(\Delta_{t,d}A_{d,n}) - 1)\Delta_{t,d}B_{t,d,n}^{\text{rot}}. \quad (27)$$

Since the discretization parameters  $\bar{A}_{t,d,n}$ ,  $\bar{B}_{t,d,n}$ , and the output parameter  $\mathbf{C}_t^{\text{rot}}$  are real-valued, the complex state transitions are decoupled into parallel real and imaginary paths. Let  $h_{t,d,n} = h_{t,d,n}^{\text{R}} + jh_{t,d,n}^{\text{I}} \in \mathbb{C}$  represent the complex latent state element. The updates are defined as:

$$h_{t,d,n}^{\text{R}} = \bar{A}_{t,d,n}h_{t-1,d,n}^{\text{R}} + \bar{B}_{t,d,n}x_{t,d}^{\text{R}}, \quad (28)$$

$$h_{t,d,n}^{\text{I}} = \bar{A}_{t,d,n}h_{t-1,d,n}^{\text{I}} + \bar{B}_{t,d,n}x_{t,d}^{\text{I}}. \quad (29)$$

The complex output  $\mathbf{y}_t = \mathbf{y}_t^{\text{R}} + j\mathbf{y}_t^{\text{I}} \in \mathbb{C}^{D_{\text{inner}}}$  is subsequently computed channel-wise as:

$$\mathbf{y}_{t,d}^{\text{R}} = \sum_{n=1}^{D_{\text{state}}} C_{t,d,n}^{\text{rot}} h_{t,d,n}^{\text{R}} + D_f x_{t,d}^{\text{R}}, \quad (30)$$

$$\mathbf{y}_{t,d}^{\text{I}} = \sum_{n=1}^{D_{\text{state}}} C_{t,d,n}^{\text{rot}} h_{t,d,n}^{\text{I}} + D_f x_{t,d}^{\text{I}}, \quad (31)$$

where  $D_f$  is the direct feedforward parameter. To execute this split-complex selective scan with high hardware efficiency, we stack the real and imaginary inputs along the batch dimension:

$$\mathbf{U}_{\text{stacked}} = [\mathbf{x}^{\text{R}}; \mathbf{x}^{\text{I}}] \in \mathbb{R}^{B_{\text{stacked}} \times D_{\text{inner}} \times N_{\text{seq}}}, \quad (32)$$

where  $B_{\text{stacked}}$  denotes the stacked batch dimension (which is twice the original batch size  $B$  due to stacking the real and imaginary parts). This allows both real and imaginary state trajectories to run in parallel in a single GPU selective scan kernel. The output  $\mathbf{y}_t$  is reconstructed by splitting the stacked batch outputs.

*d) Phase-Preserving Complex Dropout Regularization:*

To prevent overfitting in cross-environment settings, we integrate a mathematically sound **Complex Dropout** module inside the Complex Mamba blocks:

$$\text{ComplexDropout}(\mathbf{x}) = [\mathbf{x}^{\text{R}} \odot \mathbf{M}_{\text{drop}}; \mathbf{x}^{\text{I}} \odot \mathbf{M}_{\text{drop}}] \cdot \frac{1}{1-p}, \quad (33)$$

where  $\mathbf{M}_{\text{drop}} \in \{0, 1\}^D$  represents a shared binary dropout mask applied identically to both real and imaginary components, and  $p$  is the dropout rate. Using a shared mask is crucial because it ensures that phase relationships ( $\angle \mathbf{x} = \arctan(\mathbf{x}^{\text{I}}/\mathbf{x}^{\text{R}})$ ) remain unchanged when a channel is dropped, maintaining signal coherence. Complex Dropout is applied after the complex input projections, after the complex causal 1D convolution, after the output projection, and on the residual path.

The final sequence output of the  $L$ -th layer  $\mathbf{Z}_L \in \mathbb{C}^{N_{\text{seq}} \times D}$  is projected back to real-valued magnitude space to form the final encoder representation:

$$\mathbf{Z}_{\text{out}} = |\mathbf{Z}_L| = \sqrt{(\mathbf{Z}_L^{\text{R}})^2 + (\mathbf{Z}_L^{\text{I}})^2 + \eta} \in \mathbb{R}^{N_{\text{seq}} \times D}. \quad (34)$$

*C. Cross-Attention Joint-Query Mapping*

Unlike conventional CNNs that generate coordinate outputs directly via spatial pooling, Mamba encoders output sequence tokens. To map these unstructured tokens to the human skeleton, we define  $J$  learnable joint-query embeddings  $\mathbf{Q} \in \mathbb{R}^{J \times D}$ .

We employ a Multi-Head Cross-Attention (MHCA) mechanism. The queries are formed by  $\mathbf{Q}$ , while the keys and values are sourced from the local spatiotemporal sequence tokens of the encoder output  $\mathbf{M} = \mathbf{Z}_{\text{out}, 1:N_p} \in \mathbb{R}^{N_p \times D}$  (excluding the class token  $\mathbf{t}_{\text{cls}}$ ):

$$\mathbf{Z}_{\text{joint}} = \text{LN} \left( \mathbf{Q} + \text{softmax} \left( \frac{(\mathbf{Q}\mathbf{W}_Q)(\mathbf{M}\mathbf{W}_K)^T}{\sqrt{d_k}} \right) \cdot \mathbf{M}\mathbf{W}_V \right), \quad (35)$$

where  $\mathbf{W}_Q, \mathbf{W}_K, \mathbf{W}_V$  are projection matrices, and LN represents Layer Normalization. This dynamic routing allows each joint query to scan the entire spatiotemporal sequence and aggregate highly correlated subcarrier-level features.

*D. Regularized GraFormer Decoder*

The joint features  $\mathbf{Z}_{\text{joint}}$  are passed into a regularized Chebyshev Graph Convolutional Network (GCN) decoder (GraFormer [13], which builds on ChebGCN [14]) to predict coordinates while explicitly enforcing skeletal topology. Let the human body graph be defined as  $\mathcal{G} = (\mathcal{V}, \mathcal{E})$ , where vertices  $\mathcal{V}$  represent the  $J$  joints, and edges  $\mathcal{E}$  represent physical bone connections.

To prevent environmental overfitting, we implement a **GraFormer with Strong Dropout** architecture. Unlike standard implementations that restrict GCN dropout to a hardcoded baseline rate  $p_{\text{base}}$ , we propagate a strong dropout rate  $p_{\text{gen}}$  across all Chebyshev Graph Convolutional (ChebGConv)

and multi-head self-attention layers inside the decoder. A ChebGConv of order  $K_{\text{cheb}}$  updates the features:

$$\mathbf{z}^{(l+1)} = \sum_{k=0}^{K_{\text{cheb}}-1} T_k(\tilde{\mathbf{L}}) \mathbf{z}^{(l)} \mathbf{W}_k^{\text{GCN}}, \quad (36)$$

where  $\tilde{\mathbf{L}} = 2\mathbf{L}/\lambda_{\text{max}} - \mathbf{I}$  is the scaled normalized Laplacian,  $\mathbf{L} = \mathbf{I} - \mathbf{D}_{\text{deg}}^{-1/2} \mathbf{A}_{\text{adj}} \mathbf{D}_{\text{deg}}^{-1/2}$  is the normalized Laplacian,  $T_k$  is the Chebyshev polynomial of order  $k$ ,  $\mathbf{D}_{\text{deg}}$  is the degree matrix,  $\mathbf{A}_{\text{adj}}$  is the adjacency matrix, and  $\mathbf{W}_k^{\text{GCN}}$  are learnable weight matrices. The GraFormer block maps features to the predicted coordinates  $\hat{\mathbf{Y}} \in \mathbb{R}^{J \times D_{\text{coord}}}$ , where  $D_{\text{coord}}$  represents the coordinate dimension.

*E. Training Loss Function*

To optimize both absolute localization accuracy and skeletal structural integrity, the network is trained using a multi-task loss function that combines absolute coordinate loss and kinematic bone length consistency loss:

$$\mathcal{L} = \mathcal{L}_{\text{abs}} + \lambda_{\text{bone}} \mathcal{L}_{\text{bone}}, \quad (37)$$

where  $\lambda_{\text{bone}}$  is the empirical weighting coefficient. The individual loss components are defined as follows:

- 1) **Absolute Position Loss** ( $\mathcal{L}_{\text{abs}}$ ) penalizes deviations of the predicted joint coordinates  $\hat{\mathbf{Y}}_j$  from the ground-truth  $\mathbf{Y}_j$  using the Mean Squared Error (MSE):

$$\mathcal{L}_{\text{abs}} = \frac{1}{J} \sum_{j=1}^J \|\hat{\mathbf{Y}}_j - \mathbf{Y}_j\|_2^2. \quad (38)$$

- 2) **Kinematic Bone Loss** ( $\mathcal{L}_{\text{bone}}$ ) enforces anatomical constraints by minimizing the discrepancy between predicted and ground-truth bone lengths across the set of skeletal edges  $\mathcal{E}$ :

$$\mathcal{L}_{\text{bone}} = \frac{1}{|\mathcal{E}|} \sum_{(u,v) \in \mathcal{E}} \left( \|\hat{\mathbf{Y}}_u - \hat{\mathbf{Y}}_v\|_2 - \|\mathbf{Y}_u - \mathbf{Y}_v\|_2 \right)^2. \quad (39)$$

This combination of losses prevents unnatural bone stretching and maintains skeletal topology under severe cross-environment domain shifts.

### III. EXPERIMENTS

*A. Experimental Setup*

**Dataset.** We evaluate the proposed C-MambaPose framework on the MM-Fi dataset [4], which is the largest public multi-modal dataset for WiFi-based human sensing. It contains 14 daily activities performed by 40 subjects across four distinct environments. The WiFi system operates at 5 GHz with a 40 MHz bandwidth, consisting of one transmitter antenna and three receiver antennas. CSI is collected over 114 subcarriers, and consecutive frames are aggregated into samples of size  $3 \times 114 \times 10$ . Each skeletal pose is annotated with the 3D coordinates of 17 joints. Following the literature, we conduct our evaluations under Protocol 1 (focusing on the 14 daily activities, e.g., walking, jumping, sitting) and Protocol 2 (focusing on the 13

rehabilitation exercises, e.g., chest expansion, squatting, lunges). To evaluate generalization, we follow three split settings:

- **Setting 1 (Random Split - S1):** Data are randomly divided into training and testing sets with a 3:1 ratio.
- **Setting 2 (Cross-Subject Split - S2):** 32 subjects are used for training and the remaining 8 subjects for testing.
- **Setting 3 (Cross-Environment Split - S3):** Data from three environments are used for training and one for testing.

**Evaluation Metrics.** We adopt three standard metrics for 3D HPE: Mean Per Joint Position Error (MPJPE, in mm) to measure absolute joint distance; Procrustes Aligned MPJPE (PA-MPJPE, in mm) to measure structural pose accuracy; and Percentage of Correct Keypoints (PCK@20 and PCK@50) to report the ratio of joints predicted within a 20 mm or 50 mm threshold.

**Implementation Details.** Our model is implemented in PyTorch and trained on an NVIDIA RTX 4070 GPU. We use the AdamW optimizer with an initial learning rate of  $3 \times 10^{-4}$  and a weight decay of 0.02. The learning rate is decayed to near zero over 50 epochs using a cosine annealing scheduler. The batch size is 256. The kinematic bone loss weight is configured as  $\lambda_{\text{bone}} = 0.1$  (while  $\mathcal{L}_{\text{abs}}$  has a weight of 1.0). For reproducibility, we list the model hyperparameters explicitly: the Spatiotemporal Complex Mamba encoder employs  $L = 2$  complex SSM blocks with state dimension  $d_{\text{state}} = 16$ , local convolution width  $d_{\text{conv}} = 4$ , expansion factor  $E = 2$ , and complex dropout rate  $p = 0.3$ . The positional encoding is sinusoidal with a base frequency parameter  $\theta_{\text{base}} = 10,000.0$ . The cross-attention joint-query mapper uses a learnable query dimension  $d_{\text{emb}} = 256$  with 4 attention heads. The GCN decoder consists of a GraFormer with 4 graph layers, hidden dimension  $d_{\text{hid}} = 128$ , and GCN dropout rate  $p_{\text{gcn}} = 0.4$ . The Complex Dynamic Selective Kernel Convolution (Complex-DSKConv) operates with dilations [1, 2].

### B. Comparison with State-of-the-Art Methods

We compare C-MambaPose against existing state-of-the-art WiFi-based 3D HPE baselines, including MetaFi++ [2], HPE-Li [15], and DT-Pose [3]. Table I summarizes the comparisons across all three split settings.

**Quantitative Results.** As shown in Table I, C-MambaPose exhibits highly competitive performance under Setting 1 (Random Split) and Setting 2 (Cross-Subject), performing on par with existing state-of-the-art architectures. Specifically, under Setting 1, our model achieves a PA-MPJPE of **100.8 mm** (matching or slightly outperforming DT-Pose’s 101.0 mm). Under Setting 2, our model achieves a PA-MPJPE of **102.8 mm** (which is comparable to the best baseline performance).

Crucially, in the most challenging cross-environment split (Setting 3) where severe domain shifts occur across rooms, our model achieves significant improvements. C-MambaPose reduces the MPJPE to **298.5 mm** (outperforming GraphPose-Fi by 4.2 mm and DT-Pose by 34.2 mm) and achieves a competitive PCK@50 of **67.1%** and a state-of-the-art PCK@20 of **15.3%**. These improvements confirm that preserving complex phase dynamics via our Spatiotemporal Mamba and

GraFormer structure successfully prevents overfitting to specific environmental layouts.

We also observe an interesting stability pattern across the split settings: while the absolute joint coordinate error (MPJPE) degrades significantly under severe domain shift in Setting 3 (rising from 165.1 mm in S1 to 298.5 mm in S3), the Procrustes Aligned error (PA-MPJPE) remains remarkably stable (100.8 mm in S1 to 102.2 mm in S3). This indicates that while environmental multipath noise causes shifts in absolute localization coordinates, the relative skeletal structure and relative joint relationships are preserved. This supports our thesis that integrating a GCN GraFormer decoder enforces structural skeleton connectivity priors, ensuring anatomically valid pose predictions even under severe environmental shift.

**Model Complexity and Runtime Benchmarks.** Table II compares the parameter sizes, inference latency, and localization performance of different models on Setting 3.

TABLE II: Model complexity, inference latency, and performance comparisons on MM-Fi (Setting 3). The best and second-best results in each category are bolded and underlined, respectively.

Model Architecture	Params (M) ↓	Latency (ms) ↓	MPJPE ↓	PCK@50 ↑
MetaFi++ [2]	26.52	59.94	367.8	55.1
GraphPose-Fi [1]	22.43	62.61	<u>302.7</u>	<b>67.2</b>
DT-Pose [3]	<u>3.20</u>	<u>4.23</u>	332.7	58.8
HPE-Li [15]	<b>0.86</b>	<b>2.24</b>	381.1	47.8
<b>Ours</b>	3.78	25.43	<b>298.5</b>	<u>67.1</u>

Our proposed C-MambaPose achieves a highly competitive trade-off between model capacity, runtime efficiency, and localization performance. Specifically, C-MambaPose requires a highly compact parameter footprint (3.78 M parameters)-an 83.1% reduction compared to GraphPose-Fi [1] (22.43 M) and is comparable in size to DT-Pose [3] (3.20 M, which is only 18% smaller), while achieving significantly superior cross-environment performance (298.5 mm MPJPE on Setting 3, compared to 302.7 mm for GraphPose-Fi and 332.7 mm for DT-Pose) without requiring any pretraining.

Furthermore, C-MambaPose strikes an excellent balance in runtime execution. As shown in Table II, our model achieves a GPU inference latency of 25.43 ms (which is 57.6% faster than MetaFi++ [2] and 59.4% faster than GraphPose-Fi [1]), while outperforming them in cross-environment localization accuracy. We acknowledge that C-MambaPose exhibits higher latency compared to purely real-valued feedforward architectures such as DT-Pose (4.23 ms) and HPE-Li (2.24 ms). This is because the sequential selective-scan recurrence and the batch-doubling split-complex operations introduce extra recurrent computational overhead on GPU compared to plain non-recurrent CNN/MLP blocks. However, this latency increase is well within the real-time threshold (under 30 ms) and is a justified trade-off for the substantial improvement in cross-environment generalization. This confirms that by coupling the selective state-space processing of Mamba with the topological graph modeling of GraFormer, C-MambaPose achieves superior cross-domain generalization while remaining highly efficient.

TABLE I: State-of-the-art comparisons on the MM-Fi dataset (Protocol 1 and 2). The best and second-best results are bolded and underlined, respectively.

Method	Protocol 1 (Daily Actions)				Protocol 2 (Rehab Exercises)			
	PCK@20 $\uparrow$	PCK@50 $\uparrow$	MPJPE $\downarrow$	PA-MPJPE $\downarrow$	PCK@20 $\uparrow$	PCK@50 $\uparrow$	MPJPE $\downarrow$	PA-MPJPE $\downarrow$
<i>Setting 1 (Random Split):</i>								
MetaFi++ [2]	49.1	86.5	186.9	120.7	32.2	81.7	213.5	121.4
HPE-Li [15]	56.2	87.6	173.4	104.5	36.9	81.9	206.1	102.7
GraphPose-Fi [1]	<b>61.1</b>	<b>89.3</b>	<b>160.6</b>	105.0	41.0	<b>84.3</b>	<b>193.5</b>	103.3
DT-Pose [3]	59.4	88.9	165.3	<u>101.0</u>	41.4	83.5	195.6	<u>101.2</u>
<b>Ours (C-MambaPose)</b>	<u>59.6</u>	<u>89.1</u>	<u>165.1</u>	<b>100.8</b>	<b>41.6</b>	<u>83.8</u>	<u>194.8</u>	<b>99.8</b>
<i>Setting 2 (Cross-Subject Split):</i>								
MetaFi++ [2]	36.4	85.5	222.3	125.4	24.0	77.5	247.0	122.7
HPE-Li [15]	38.2	82.8	228.6	106.8	26.9	78.0	242.6	101.9
GraphPose-Fi [1]	<b>44.2</b>	86.3	<b>210.5</b>	<u>105.5</u>	<b>31.8</b>	<b>80.5</b>	<b>227.6</b>	102.8
DT-Pose [3]	41.9	86.7	213.0	105.6	28.5	78.5	238.3	<u>101.1</u>
<b>Ours (C-MambaPose)</b>	<u>42.2</u>	<b>87.1</b>	<u>211.5</u>	<b>102.8</b>	<u>28.8</u>	<u>78.8</u>	<u>236.8</u>	<b>100.8</b>
<i>Setting 3 (Cross-Environment Split):</i>								
MetaFi++ [2]	9.3	55.1	367.8	121.0	<u>5.3</u>	45.9	360.2	117.2
HPE-Li [15]	4.3	47.8	381.1	110.3	4.2	40.3	378.2	104.0
GraphPose-Fi [1]	<u>12.9</u>	<b>67.2</b>	<u>302.7</u>	<u>103.0</u>	<u>5.3</u>	42.0	373.4	105.4
DT-Pose [3]	10.7	58.8	332.7	105.1	4.4	<u>49.7</u>	<u>338.3</u>	<u>102.0</u>
<b>Ours (C-MambaPose)</b>	<b>15.3</b>	<u>67.1</u>	<b>298.5</b>	<b>102.2</b>	<b>8.4</b>	<b>56.9</b>	<b>317.6</b>	<b>101.1</b>

### C. Ablation Study

To evaluate the effectiveness of the individual components of C-MambaPose, we conduct comprehensive ablation studies on Setting 3 (Cross-Environment) of the MM-Fi dataset.

**Architecture Components.** Table III analyzes the impact of the complex-valued formulation, Complex-DSKConv, GraFormer decoder, the placement of the magnitude projection bottleneck, the Rotary Position Embedding (RoPE), and the Shared-Mask Complex Dropout.

TABLE III: Ablation study of model architectural components on MM-Fi (Setting 3). The ‘‘Phase Bottleneck (Mag before Mamba)’’ configuration projects complex features to real magnitude values before entering the spatiotemporal Mamba layers.

Configuration	MPJPE (mm) $\downarrow$	PA-MPJPE (mm) $\downarrow$
Ours (Full Model)	<b>298.5</b>	<b>102.2</b>
w/o Complex Representation	365.5	103.5
w/o Complex-DSKConv	339.5	103.9
w/o GraFormer (MLP decoder)	358.9	103.2
Phase Bottleneck (Mag before Mamba)	335.0	102.3
w/o Rotary Position Embedding (RoPE)	312.4	102.9
w/o Shared-Mask Complex Dropout	321.8	103.1

Replacing our complex-valued pipeline with a standard real-valued amplitude-only input leads to a degraded MPJPE of 365.5 mm, highlighting that phase information is crucial for tracking Doppler shifts in unseen domains. Furthermore, removing the Complex-DSKConv module yields a degraded MPJPE of 339.5 mm, proving that a dynamic multi-scale receptive field is essential to capture varied motion speeds. Replacing the GraFormer GCN with an MLP decoder degrades performance to 358.9 mm, demonstrating the regularizing effect of joint connectivity priors. Projecting complex features to real magnitude before sequential processing (Phase Bottleneck) leads to a degraded MPJPE of 335.0 mm, validating that preserving phase relations inside the Mamba sequence blocks is vital.

Additionally, removing the Rotary Position Embedding (RoPE) from state transitions degrades the MPJPE to 312.4 mm, confirming that explicitly encoding relative spatiotemporal token distances is crucial for tracking sequential body movements. Finally, removing the Shared-Mask Complex Dropout (i.e., applying independent dropout masks to real

and imaginary channels) degrades the MPJPE to 321.8 mm. This is because independent masks disrupt the phase angle relationships ( $\angle x = \arctan(x^I/x^R)$ ) between the real and imaginary channels, introducing random phase distortion that degrades physical signal coherence and generalization.

**Impact of Kinematic Bone Loss.** Table IV evaluates the model under different values of the kinematic bone loss coefficient  $\lambda_{\text{bone}}$  when added to the absolute position loss baseline  $\mathcal{L} = \mathcal{L}_{\text{abs}} + \lambda_{\text{bone}}\mathcal{L}_{\text{bone}}$ .

TABLE IV: Ablation of kinematic loss coefficient  $\lambda_{\text{bone}}$  on MM-Fi (Setting 3).

Loss Configuration	MPJPE (mm) $\downarrow$	PA-MPJPE (mm) $\downarrow$
$\lambda_{\text{bone}} = 0$ (MPJPE Loss only)	314.3	102.4
$\lambda_{\text{bone}} = 0.1$ (Ours)	<b>298.5</b>	<b>102.2</b>
$\lambda_{\text{bone}} = 0.5$	302.5	103.0

Without the bone length constraint ( $\lambda_{\text{bone}} = 0$ ), the model achieves 314.3 mm MPJPE. Introducing the constraint with  $\lambda_{\text{bone}} = 0.1$  guides the model to maintain physical skeletal symmetry, yielding the best results. However, setting the weight too high ( $\lambda_{\text{bone}} = 0.5$ ) overly penalizes joint movements and restricts positional flexibility, worsening the errors to 302.5 mm.

## IV. CONCLUSION AND DISCUSSION

In this paper, we presented C-MambaPose, a physics-informed complex-valued Mamba-GraFormer hybrid framework for robust WiFi-based 3D human pose estimation (HPE). By designing a phase-preserving complex patchification pipeline using Complex-ModReLU and Complex-DSKConv, C-MambaPose successfully retains the physical phase relationship of WiFi signals to capture fine-grained Doppler frequency shifts representing body movement. We employed a Spatiotemporal Complex Mamba encoder to model long-range sequential temporal dynamics and mapped unstructured sequence tokens to joints using a cross-attention joint-query mapping module. Furthermore, we integrated a GraFormer GCN decoder to explicitly model human skeletal topology, regularizing the model to predict anatomically coherent poses and prevent unnatural bone stretching.

Extensive evaluations on the MM-Fi dataset demonstrate that C-MambaPose achieves competitive or superior performance

to state-of-the-art baselines across all settings, setting a new state-of-the-art on the challenging cross-environment split (Setting 3) and leading on the PA-MPJPE metric across all settings. Notably, in the challenging cross-environment split, it significantly outperforms recent baselines with a highly compact parameter size, confirming its high efficiency and generalization.

**Future Work.** Although C-MambaPose represents a significant step forward, there are several avenues for future research. First, we plan to extend this framework to multi-person pose estimation, which requires modeling the spatial overlapping of multiple WiFi reflection paths. Second, we aim to investigate transfer learning and domain adaptation techniques to further reduce the error when testing in completely unseen rooms. Finally, we plan to deploy C-MambaPose on edge computing devices to validate its real-time performance and practicality in smart home applications.

## REFERENCES

- [1] J. Chen, Y. Qu, R. Tang, and D. Slock, "Graph-based 3d human pose estimation using wifi signals," in *ICASSP 2026-2026 IEEE International Conference on Acoustics, Speech and Signal Processing (ICASSP)*. IEEE, 2026, pp. 19 992–19 996.
- [2] Y. Zhou, H. Huang, S. Yuan, H. Zou, L. Xie, and J. Yang, "Metafi++: Wifi-enabled transformer-based human pose estimation for metaverse avatar simulation," *IEEE Internet of Things Journal*, vol. 10, no. 16, pp. 14 128–14 136, 2023.
- [3] Y. Chen, J. Guo, S. Guo, J. Zhou, and D. Tao, "Towards robust and realistic human pose estimation via wifi signals," *arXiv preprint arXiv:2501.09411*, 2025.
- [4] J. Yang, H. Huang, Y. Zhou, X. Chen, Y. Xu, S. Yuan, H. Zou, C. X. Lu, and L. Xie, "Mm-fi: Multi-modal non-intrusive 4d human dataset for versatile wireless sensing," in *Thirty-seventh Conference on Neural Information Processing Systems Datasets and Benchmarks Track*, 2023. [Online]. Available: <https://openreview.net/forum?id=1uAsASS1th>
- [5] Y. Dao, L. Zhang, H. Liu, H. Zhang, and W. Wang, "Wiflow: A lightweight wifi-based continuous human pose estimation network with spatio-temporal feature decoupling," 2026. [Online]. Available: <https://arxiv.org/abs/2602.08661>
- [6] N. Zheng, Y. Li, S. Jiang, Y. Li, R. Yao, C. Dong, T. Chen, Y. Yang, Z. Yin, and Y. Liu, "Adawifi, collaborative wifi sensing for cross-environment adaptation," *IEEE Transactions on Mobile Computing*, vol. 24, no. 2, pp. 845–858, 2025.
- [7] Y. Huang, J. Liu, X. Shi, S. Zhao, T. Mi, and R. C. Qiu, "Sensemamba: A general lightweight state-space model for wireless human sensing," *IEEE Sensors Journal*, vol. 25, no. 8, pp. 13 859–13 870, 2025.
- [8] J. Liu, Y. Huang, X. Shi, X. Ren, T. Mi, and R. C. Qiu, "Tf-mamba: A lightweight state-space model for wi-fi-based human activity recognition," *IEEE Sensors Journal*, vol. 25, no. 13, pp. 23 184–23 194, 2025.
- [9] A. Djuhera, H. Gacanin, and H. Boche, "Mambacsp: Hybrid-attention state space models for hardware-efficient channel state prediction," 2026. [Online]. Available: <https://arxiv.org/abs/2604.21957>
- [10] A. Lahoti, K. Li, B. Chen, C. Wang, A. Bick, J. Z. Kolter, T. Dao, and A. Gu, "Mamba-3: Improved sequence modeling using state space principles," in *The Fourteenth International Conference on Learning Representations*, 2026. [Online]. Available: <https://openreview.net/forum?id=HwCvaJOiCj>
- [11] C. Trabelsi, O. Bilaniuk, Y. Zhang, D. Serdyuk, S. Subramanian, J. F. Santos, S. Mehri, N. Rostamzadeh, Y. Bengio, and C. J. Pal, "Deep complex networks," in *International Conference on Learning Representations*, 2018. [Online]. Available: <https://openreview.net/forum?id=H1T2hmZAb>
- [12] X. Li, W. Wang, X. Hu, and J. Yang, "Selective kernel networks," in *2019 IEEE/CVF Conference on Computer Vision and Pattern Recognition (CVPR)*, 2019, pp. 510–519.
- [13] W. Zhao, W. Wang, and Y. Tian, "Graformer: Graph-oriented transformer for 3d pose estimation," in *Proceedings of the IEEE/CVF conference on computer vision and pattern recognition*, 2022, pp. 20 438–20 447.
- [14] M. Defferrard, X. Bresson, and P. Vandergheynst, "Convolutional neural networks on graphs with fast localized spectral filtering," in *Proceedings of the 30th International Conference on Neural Information Processing Systems*, ser. NIPS'16. Red Hook, NY, USA: Curran Associates Inc., 2016, p. 3844–3852.
- [15] T. D. Gian, T. Dac Lai, T. Van Luong, K.-S. Wong, and V.-D. Nguyen, "Hpe-li: Wifi-enabled lightweight dual selective kernel convolution for human pose estimation," in *Computer Vision – ECCV 2024*, A. Leonardis, E. Ricci, S. Roth, O. Russakovsky, T. Sattler, and G. Varol, Eds. Cham: Springer Nature Switzerland, 2025, pp. 93–111.